

RESEARCH ARTICLE

Interface engineering and characterization at the atomic-scale of pure and mixed ion layer gas reaction buffer layers in chalcopyrite thin-film solar cells

Oana Cojocaru-Mirédin^{1*}, Yanpeng Fu², Aleksander Kostka¹, Rodrigo Sáez-Araoz², Andreas Beyer³, Nikolai Knaub³, Kerstin Volz³, Christian-Herbert Fischer² and Dierk Raabe¹

¹ Max-Planck-Institut für Eisenforschung, Max-Planck-Str. 1, 40237 Düsseldorf, Germany

² Helmholtz-Zentrum Berlin für Materialien und Energie, Institute of Heterogeneous Materials Systems, Hahn-Meitner-Platz 1, D-14109 Berlin, Germany

³ Philipps-Universität Marburg, Hans-Meerwein-Straße, D-35032 Marburg, Germany

ABSTRACT

In this work, we investigate the p–n junction region for two different buffer/Cu(In,Ga)(Se,S)₂ (CIGSSe) samples having different conversion efficiencies (the cell with pure In₂S₃ buffer shows a lower efficiency than the nano-ZnS/In₂S₃ buffered one). To explain the better efficiency of the sample with nano-ZnS/In₂S₃ buffer layer, combined transmission electron microscopy, atom probe tomography, and X-ray photoelectron spectroscopy studies were performed. In the pure In₂S₃ buffered sample, a CuIn₃Se₅ ordered-defect compound is observed at the CIGSSe surface, whereas in the nano-ZnS/In₂S₃ buffered sample no such compound is detected. The absence of an ordered-defect compound in the latter sample is explained either by the presence of the ZnS nanodots, which may act as a barrier layer against Cu diffusion in CIGSSe hindering the formation of CuIn₃Se₅, or by the presence of Zn at the CIGSSe surface, which may disturb the formation of this ordered-defect compound. In the nano-ZnS/In₂S₃ sample, Zn was found in the first monolayers of the absorber layer, which may lead to a downward band bending at the surface. This configuration is very stable (Fermi level pinning at the conduction band, as observed for Cd in Cu(In,Ga)Se₂) and reduces the recombination rate at the interface. This effect may explain why the sample with ZnS nanodots possesses a higher efficiency. This work demonstrates the capability of correlative transmission electron microscopy, atom probe tomography, and X-ray photoelectron spectroscopy studies in investigating buried interfaces. The study provides essential information for understanding and modeling the p–n junction at the nanoscale in CIGSSe solar cells. Copyright © 2014 John Wiley & Sons, Ltd.

KEYWORDS

ZnS nanodots; In₂S₃ alternative buffer layer; ILGAR; ordered-defect compound; atom probe tomography; transmission electron microscopy; X-ray photoelectron spectroscopy

*Correspondence

Oana Cojocaru-Mirédin, Max-Planck-Institut für Eisenforschung, Max-Planck-Str. 1, 40237 Düsseldorf, Germany.

E-mail: o.cojocaru-miredin@mpie.de

Received 30 May 2013; Revised 13 November 2013; Accepted 22 January 2014

1. INTRODUCTION

Cu(In,Ga)(S,Se)₂ (CIGSSe)-based thin-film solar cells are a promising alternative to the silicon photovoltaics technology having achieved efficiencies of more than 20% at lab scale [1]. The thin-film layer stack of the cells consists of soda lime glass substrate, Mo (back contact), p-CIGSSe (absorber), n-buffer, and i-ZnO + n-ZnO + Ni/Al grid (front contact). The merely 20–60 nm thick buffer is crucial for the device performance, because it forms together with the absorber the p–n junction, which is necessary for the charge separation.

The functions of this buffer are manifold. For the present work, we mention only the requirement to form a good band alignment and a low defect density at the p–n junction which is necessary to reduce the charge carrier recombination.

Nowadays, toxic CdS is the standard buffer material that is used in commercial products. This buffer is deposited by chemical bath deposition (CBD) [2,3], which produces huge amounts of cadmium containing liquid waste. Great efforts are being made in the community to replace not only the toxic material, but also the liquid CBD process, which is not adequate for a dry production line.

A compilation of the current development of the buffer layers is given by Naghavi *et al.* [4].

Spray-ion layer gas reaction (ILGAR) is a sequential and cyclic chemical method for depositing metal sulfide thin layers [5–7]. In the first process step, a metal oxide precursor film is deposited by ultrasonic spraying following an aerosol-assisted chemical vapor deposition mechanism [8]. In the second step, the precursor is converted by the reactant gas H_2S to the metal sulfide. Repetition of this process cycle enables a very good control of the layer thickness. The ILGAR process is flexible as it enables tuning the material composition as well as the deposition of mixed or multi-layers. Moreover this technique allows the adjustment of important properties, such as conductivity, band gap, and crystallite size.

Solar cells based on ILGAR In_2S_3 buffer layer deposited on CIGSSe absorbers had already reached efficiencies up to 16.8% (in-house) and 16.1% (certified), which is a record for In_2S_3 buffered solar cell, regardless of the buffer deposition technique [9]. However, photoluminescence experiments revealed clearly lower recombination rates for ZnS and CdS than for In_2S_3 [10]. Due to the low conductivity of ZnS, buffer layers based on this material are not an optimal choice. In the present case, the ZnS phase has a form of either a very thin layer or preferably separated nanodots (NDs). Indeed, a thick ZnS layer would lead to an unfavorable band line-up with a too large spike because of the wide band gap of ZnS [11]. Therefore, Fu *et al.* [12,13] developed a new buffer layer composed by ZnS NDs covered by an In_2S_3 layer. Indeed, this mixed ZnS- In_2S_3 buffer layer shows better open-circuit voltage (V_{oc}) and efficiency (up to 1.5% abs. higher compared with pure In_2S_3 buffer). The effect is explained in terms of defect passivation by the ZnS NDs and charge carrier transport via the In_2S_3 point contacts [13].

In the present work, we characterize pure In_2S_3 and combined nano-ZnS/ In_2S_3 buffers using correlative high-resolution scanning transmission electron microscopy (HRSTEM), laser-assisted atom probe tomography (APT) [14], and X-ray photoelectron spectroscopy (XPS) [13] studies. The aim of this study is to understand the difference in nanoscopic structure and composition of the p–n junction between these two buffers in order to explain the higher efficiency of mixed ZnS- In_2S_3 buffer layer.

2. EXPERIMENTAL

2.1. Cell fabrication

The deposition of ZnS and In_2S_3 layers is performed by the two-step cyclical spray-ILGAR process [12,15]. Within a cycle, a zinc-containing or indium-containing precursor layer is first deposited by an aerosol-assisted chemical vapor deposition type reaction and then converted to zinc or indium sulfide by the introduction of H_2S (e.g., $2\text{InCl}_3 + 3\text{H}_2\text{S} \rightarrow \text{In}_2\text{S}_3 + 6\text{HCl}$). Aqueous zinc acetylacetonate solution or alcoholic indium chloride solution is used respectively for the deposition of each layer. The standard 15 nm thick In_2S_3 layer is produced within six process cycles, whereas the ZnS

ND layer is produced within 20 cycles. The typical distance between the dots is below 5 nm, which is several orders of magnitude less than the minority carrier diffusion lengths in chalcopyrite solar cells [16]. It is important that the minority carrier (the electrons here) has a diffusion length enough to travel to the nearest point contact (i.e., the In_2S_3 layer).

Both layers are deposited onto commercially available CIGSSe absorbers (AVANCIS GmbH & Co. KG), which are kept at 225 °C during the deposition process. The cells are completed with 70–100 nm i-ZnO, 400–500 nm ZnO:Al layers, and Ni/Al contact grids using standard RF sputtering. We note here that for the APT measurements, the In_2S_3 layer is produced using 50 subsequent process cycles (around 200 nm thick layer) in order to preserve the p–n junction during the sample preparation by focused-ion-beam (FIB).

2.2. Device characterization

The efficiency of the devices was measured in lab with an Oriel solar simulator (approx. AM 1.5) at 1000 W m^{-2} .

The microstructure of the In_2S_3 and nano-ZnS/ In_2S_3 buffer layers was studied using two JEOL JEM-2200FS HRTEMs operated at 200 kV: double-Cs corrected instrument at University of Marburg and an analytical instrument at the Max-Planck Institute for Iron Research in Düsseldorf. The TEM lamellas containing the region of interest necessary for the (HR)TEM studies were prepared using a dual beam FIB (FEI Helios Nanolab 600i). In order to avoid any contaminations or damages due to the Ga^+ beam, these TEM lamellas were finally cleaned using a very low-kV Ga^+ beam (500 eV).

APT experiments were performed with a local electrode atom probe (LEAPTM 3000× HR, Cameca Instruments), applying laser pulses of 532 nm wavelength, 12 ps pulse length, and an energy of 0.1 nJ per pulse at a repetition rate of 100 kHz. The specimen base temperature was about 60 K. Tip samples, necessary for the APT measurements, were prepared using a dual beam FIB (FEI Helios Nanolab 600i) according to the procedure described in [17]. To minimize beam damage, a low energy (2 keV) Ga beam was used at the final ion-milling stage.

For the XPS depth profile measurement, the ZnS nanodots (NDs) are incrementally removed from the absorber surface by etching in 50 mL 2% aqueous HCl solution [13]. XPS spectra were obtained with a CLAM4 (Thermo VG Scientific) concentric semi-hemispherical analyzer and an Al $K\alpha$ /Mg $K\alpha$ X-ray tube.

3. RESULTS

3.1. Electrical properties of pure In_2S_3 and nano-ZnS/ In_2S_3 buffered Cu(In,Ga)(Se,S)₂ solar cells

Table I shows the best cell performance of pure In_2S_3 and nano-ZnS/ In_2S_3 buffered CIGSSe solar cells used in this investigation. All absorbers stem from the same batch.

Table 1. Best cell performance of pure In_2S_3 and nano-ZnS/ In_2S_3 buffered Cu(In,Ga)(Se,S) $_2$ solar cells of this investigation.

Buffer	η [%]	V_{oc} [mV]	J_{sc} [mA/cm 2]	FF [%]
Pure In_2S_3	14.7	554	38.5	69.1
Nano-ZnS/ In_2S_3	15.7	571	38.8	70.3

The substrate size used is $2.5 \times 2.5 \text{ cm}^2$ with a cell size of 0.5 cm^2 ; η : efficiency, V_{oc} : open-circuit voltage; J_{sc} : short circuit current, FF : fill factor.

Compared with the pure In_2S_3 buffer, the addition of ZnS NDs between the absorber surface and the In_2S_3 layer helps to increase the V_{oc} and fill factor (FF) of the solar cell and further raises its efficiency (η). The improvement of the cell performance is explained by a controlled *passivation/point contact effect*: ZnS NDs reduce the recombination activity at the absorber/buffer heterointerface (*passivation*), while the In_2S_3 forms *point contacts* for the charge carrier transport (knowing that ZnS has a poor electrical conductivity).

Besides the electrical properties, structural and chemical (diffusion processes) properties may also influence the performance of the absorber/buffer interface. Therefore, in the next two sections, we will focus on structural and chemical properties, in order to understand a possible electrical-structural-chemical correlation for these two different buffer layers.

3.2. Structural properties of pure In_2S_3 and nano-ZnS/ In_2S_3 buffer layers

The nanostructure of both pure In_2S_3 and nano-ZnS/ In_2S_3 buffer layers was studied using a combination of analytical TEM (high-angle annular dark field (HAADF)), electron diffraction pattern (DP), energy dispersive X-ray spectroscopy (EDX), and high-resolution (HR)STEM. Figure 1 shows the In_2S_3 /CIGSSe interface, corresponding DP, and EDX line profile. The In_2S_3 layer has a thickness of about 200 nm and consists of nanocrystalline grains (20–60 nm size). The DP (Figure 1(b)) reveals that most of the In_2S_3 have the $[001]_{\text{In}_2\text{S}_3} \parallel [100]_{\text{CIGSSe}}$ orientation relationship with the CIGSSe absorber layer. However, there are some randomly oriented crystals visible on the DP as ring (like that of (213) plane). The rather weak intensity of that ring suggests that randomly oriented crystallites are low volume fraction of the In_2S_3 layer.

The microstructure and the corresponding DP and EDX line profile through the In_2S_3 /ZnS/CIGSSe interface is presented on Figure 2. The In_2S_3 layer appears similar to that of In_2S_3 /CIGSSe (nanocrystalline layer of 200 nm thickness), however, small ZnS dots (darker regions) are present in the In_2S_3 adjacent to the interface.

In order to identify the phases shown on the complex DP (Figure 2(b)), individual patterns were acquired from the main components (Figure 2(c) and (d)) and simulated (Figure 2(e)–(g)). The results reveal a

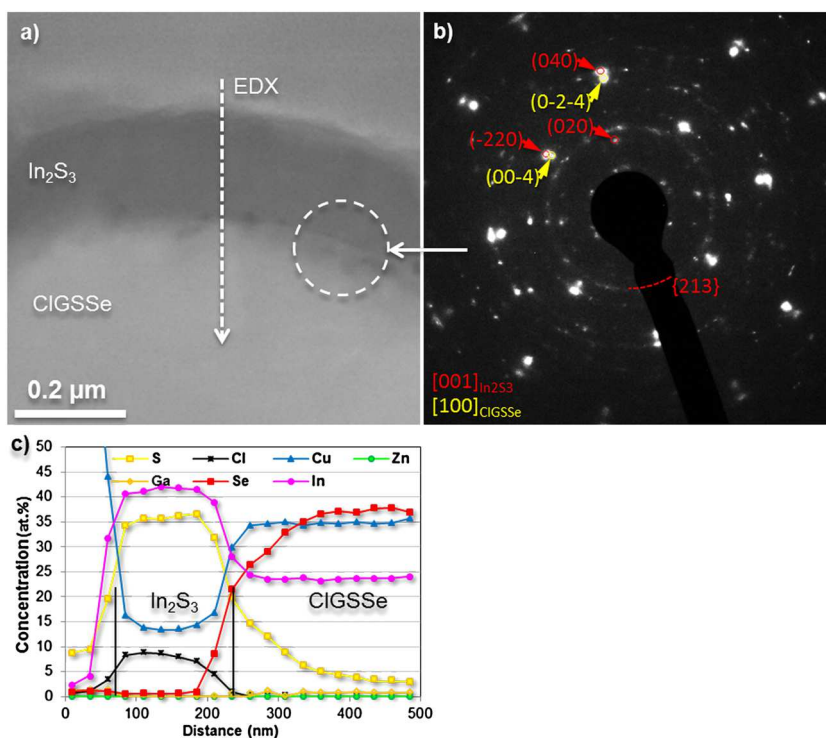


Figure 1. (a) High-angle annular dark field micrograph of a In_2S_3 /Cu(In,Ga)(Se,S) $_2$ (CIGSSe) interface. (b) Corresponding diffraction pattern from the highlighted region. (c) Energy dispersive X-ray spectroscopy (EDX) line profile through In_2S_3 layer and CIGSSe surface.

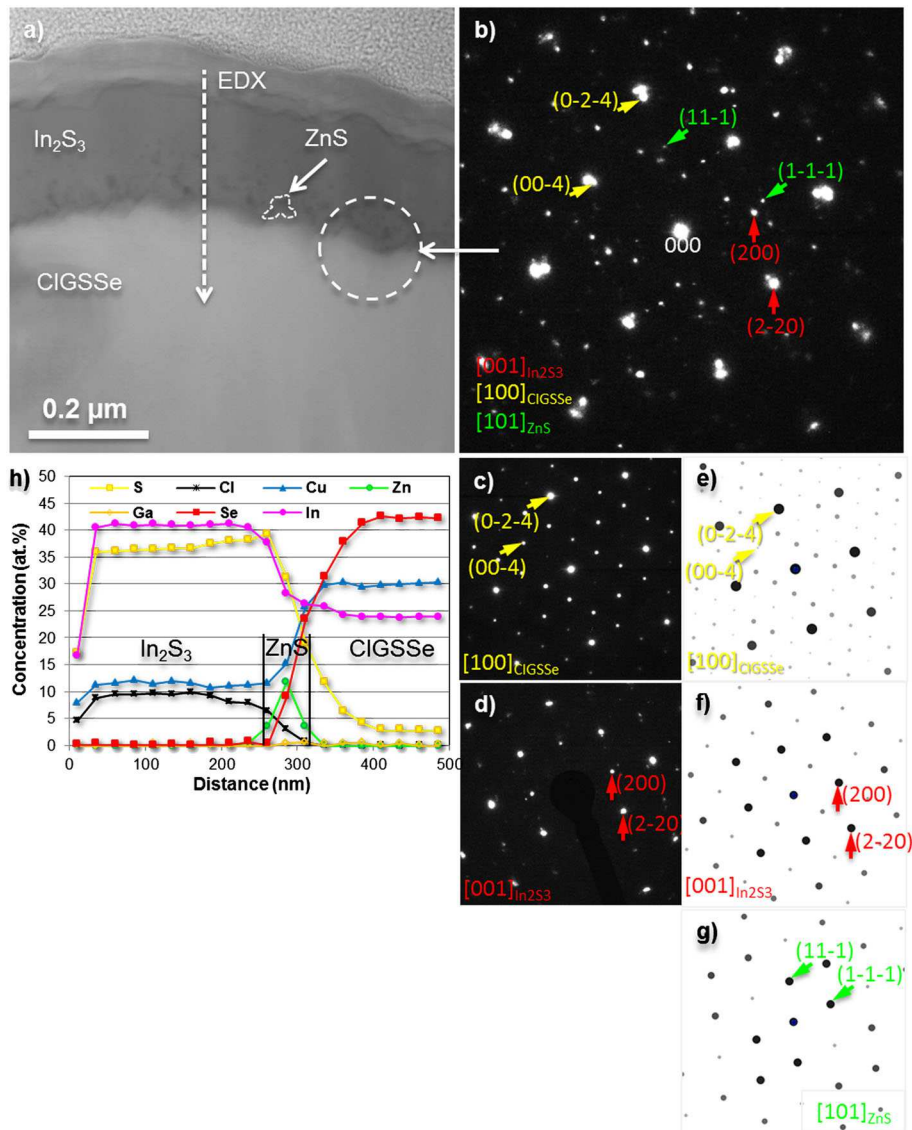


Figure 2. (a) High-angle annular dark field micrograph of a $\text{In}_2\text{S}_3/\text{ZnS}/\text{Cu}(\text{In,Ga})(\text{Se,S})_2$ (CIGSSe) interface. Diffraction pattern from the (b) highlighted region, (c) CIGSSe, and (d) In_2S_3 . (e)–(g) simulated diffraction patterns of all the phases present on the interface. (h) EDX line profile through In_2S_3 , ZnS, and CIGSSe surface.

$[001]_{\text{In}_2\text{S}_3} \parallel [101]_{\text{ZnS}} \parallel [100]_{\text{CIGSSe}}$ orientation relationship between the ZnS NDs, buffer, and absorber layers. The In_2S_3 and CIGSSe layers keep the same orientation relationship as the pure In_2S_3 sample.

The structural details of the $\text{In}_2\text{S}_3/\text{CIGSSe}$ interfaces with and without ZnS NDs were also studied using HRSTEM. Figure 3(a) shows the $\text{In}_2\text{S}_3/\text{CIGSSe}$ interface in high resolution and corresponding fast Fourier transform. The presence of a layer between the buffer and absorber layers (darker than CIGSSe, see Figure 3(a)) is highlighted. This layer has a very inhomogeneous thickness (between 1 and 10 nm), and it is coherent with the absorber layer. Analysis of the DPs obtained from the CIGSSe absorber and the CIGSSe surface region (Figure 3 (b) and (c), respectively) reveals that this layer has the

same chalcopyrite structure as the CIGSSe layer. Yan *et al.* [18] earlier observed the formation of such ordered-defect compound (ODC) or ordered-vacancy compound (OVC) structure that in our case can be identified by the presence of additional weak spots (indicated by arrows in Figure 3(c)) and the inserted Fourier transform Figure 3(a)). Indeed the structure of CuIn_3Se_5 is derived from that of CuInSe_2 with an ordered array of Cu vacancies or $(2V_{\text{Cu}} + \text{In}_{\text{Cu}}^{2+})$ defect pairs. We note here that this layer is not an artificial layer due to the overlap between CIGSSe and In_2S_3 . This latter affirmation is based first on the fact that the DP corresponds to ODC and not to an overlap between CIGSSe and In_2S_3 , and second, the thickness of the layer is very inhomogeneous, which do not correspond to typical overlapping between In_2S_3 and CIGSSe.

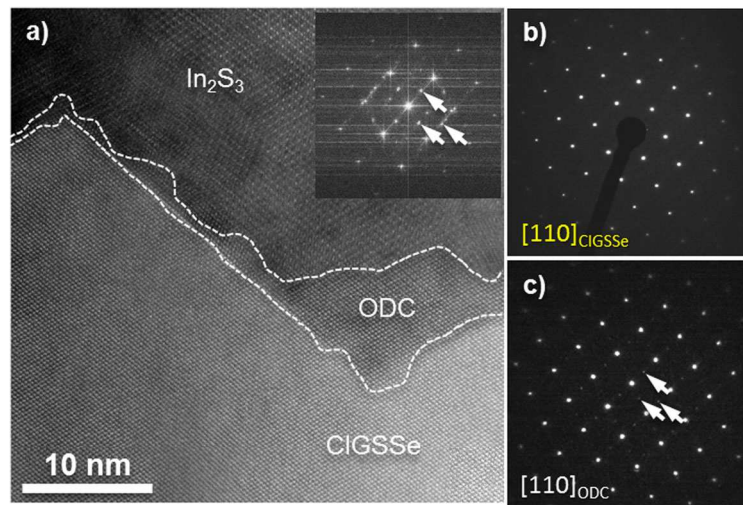


Figure 3. (a) High-resolution high-angle annular dark field image of $\text{In}_2\text{S}_3/\text{Cu}(\text{In,Ga})(\text{Se,S})_2$ (CIGSSe) interface and the corresponding fast Fourier transform. (b) and (c) Diffraction patterns obtained for the CIGSSe phase and for the ordered-defect compound (ODC), respectively. White arrows indicate an ordered-vacancy compound (OVC) phase.

Figure 4 presents the $\text{In}_2\text{S}_3/\text{ZnS}/\text{CIGSSe}$ interface region. Contrary to the $\text{In}_2\text{S}_3/\text{CIGSSe}$ interface, no ODC phase is detected. The ZnS NDs present at the $\text{In}_2\text{S}_3/\text{CIGSSe}$ interface are not clearly separated from one another as it is shown in Figure 4, and they are found in a 3–4 nm thick region. The appearance of the ZnS NDs in the form of continuous layer is due to the fact that 50 nm thick TEM lamellae contains around 10 dots in depth, and therefore the HR-ADF image obtained shows a superposition of several NDs.

The presence of a Zn-rich layer between the buffer and absorber layers was observed using EDX (Figure 2(c), EDX map not shown here), whereas the EDX line profile

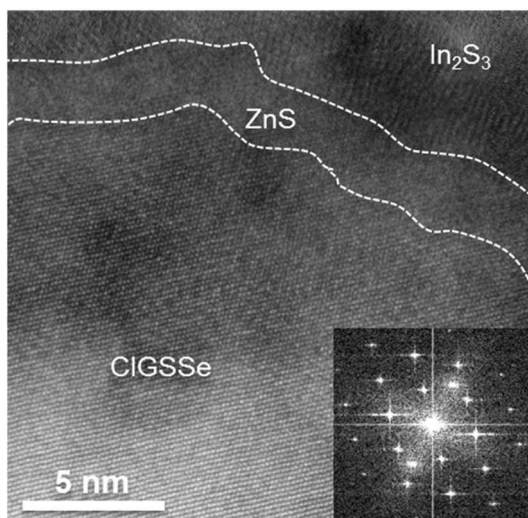


Figure 4. High-resolution high-angle annular dark field image of $\text{In}_2\text{S}_3/\text{ZnS}/\text{Cu}(\text{In,Ga})(\text{Se,S})_2$ (CIGSSe) interface and the corresponding fast Fourier transform.

performed for the pure In_2S_3 sample shows no Zn-rich layer at the $\text{In}_2\text{S}_3/\text{CIGSSe}$ interface as expected (Figure 1(c)). As for HR-ADF image (Figure 4), single NDs cannot be resolved in EDX, knowing that within the depth of the lamella, we have a superposition of several NDs. We note here that the quantitative EDX measurements were performed at relatively thick regions (~100 nm) to minimize the effect of the Ga-beam damages (created at 500 eV during the sample preparation) on the composition. Furthermore, due to resolution limit of the EDX, composition information regarding the ZnS NDs or the ODC (OVC) could not be determined. Therefore, APT studies were required to determine the absolute composition value of ZnS NDs and ODC observed at p–n junction for pure In_2S_3 and nano-ZnS/ In_2S_3 samples.

3.3. Compositional gradients at $\text{In}_2\text{S}_3/\text{CIGSSe}$ and $\text{In}_2\text{S}_3/\text{nano-ZnS}/\text{CIGSSe}$ interfaces

The APT technique, a combination of time of flight mass spectrometry and ion projection microscopy, allows three-dimensional elemental mapping with near-atomic resolution and high detection sensitivity, thus enabling accurate atomic-scale tomographic chemical analyses of buried interfaces [14]. Recent APT studies were performed on CuInSe_2 (CIS) and CIGS solar cells containing CdS buffer [19–21]. These APT studies clearly revealed compositional gradients at the CdS/CI(G)S interface (Cu-depleted and Cd-enriched CIGS surface), but also the impurity distribution (mainly Na and O) within this interface. We note here that by APT only specific regions of maximum $100 \times 100 \times 500 \text{ nm}^3$ can be analyzed. This means that several analyses on different regions of the same sample are necessary in order to build-up a more general conclusion.

Figure 5 shows the proximity histogram (or proxigram) (for more details, see [22]) obtained from the APT data across the p–n junction for pure In_2S_3 sample (Figure 5(a)) and for nano-ZnS/ In_2S_3 sample (Figure 5(b)). The interface, relative to which the proxigram is constructed, can be defined in terms of an iso-concentration threshold value. As explained by Yoon *et al.* [23], the threshold value for the interface is located at the steepest point of the concentration gradient of a chosen profile in the proxigram. In Figures 5(a) and (b), the steepest points of the sulfur S-shaped profiles are 43 and 40 at.% S, respectively.

In Figure 5(a), the region between -1 nm and $+1\text{ nm}$ represents the mixed interface region. As shown in this diagram, the $\text{In}_2\text{S}_3/\text{CIGSSe}$ interface is rather diffuse ($\sim 2\text{ nm}$ in width), which could be partly due to different evaporation fields of In_2S_3 and CIGSSe layer and hence, to a corresponding reconstruction artifact [24]. On the other hand, as shown in Table II, the In_2S_3 layer contains quite a high amount of Cu (6.8 at.%) and Se (4.2 at.%), which indicates that during the ILGAR deposition of In_2S_3 at 225°C , Cu and Se diffuse from the CIGSSe layer into In_2S_3 . We note here that the average composition of the In_2S_3 layer in Figure 5(a) exhibits a slight deviation from the expected nominal composition (Table II). This is due to the overlapping mass-to-charge peaks, namely between $^{65}\text{S}_2^{1+}$ and $^{65}\text{Cu}^{1+}$ and between $^{97}\text{S}_3^{1+}$ and $^{97}\text{CuS}^{1+}$, which cannot be deconvoluted in the composition profile. This leads to an overestimation of Cu in In_2S_3 and CIGSSe layers,

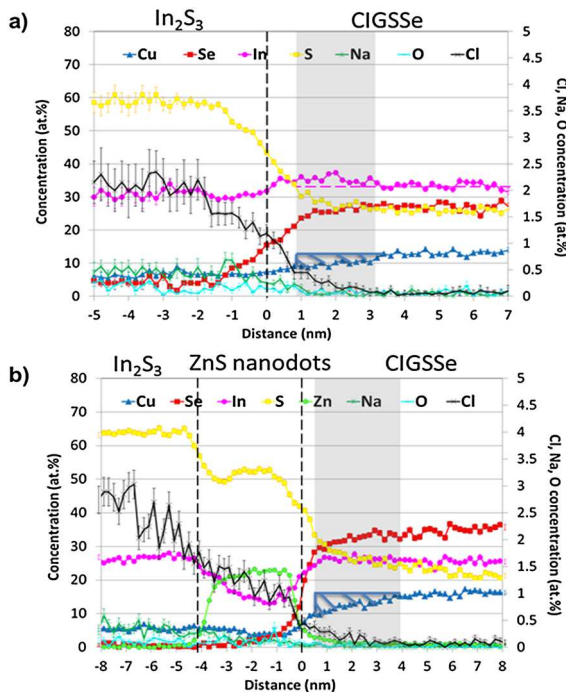


Figure 5. Proximity histogram across (a) $\text{In}_2\text{S}_3/\text{Cu}(\text{In,Ga})(\text{Se,S})_2$ (CIGSSe) using an iso-concentration threshold value of 43 at.% S and (b) $\text{In}_2\text{S}_3/\text{ZnS}/\text{CIGSSe}$ using an iso-concentration threshold value of 40 at.% S.

Table II. Chemical composition of different layers (pure buffer, mixed buffer, and absorber) obtained from APT mass-to-charge spectra after decomposition of overlapping mass peaks.

Sample	Layer	In (at.%)	S (at.%)	Zn (at.%)	Cu (at.%)	Ga (at.%)	Se (at.%)	Na (at.%)	O (at.%)	Cl (at.%)
Pure In_2S_3	In_2S_3	28.2 ± 0.5	58.0 ± 0.6	-	6.8 ± 0.3	-	4.2 ± 0.3	0.3 ± 0.06	0.1 ± 0.03	2.2 ± 0.2
	CIGSSe	32.0 ± 0.06	3.6 ± 0.02	-	21.4 ± 0.05	0.03 ± 0.002	42.7 ± 0.06	0.004 ± 0.0008	0.02 ± 0.01	-
nano-ZnS/ In_2S_3	In_2S_3	26 ± 0.3	64 ± 0.3	-	5.4 ± 0.1	-	-	0.2 ± 0.03	0.1 ± 0.02	4 ± 0.1
	Mixed ZnS/ In_2S_3	15.5 ± 0.6	50.4 ± 0.8	-	4.9 ± 0.3	-	3.1 ± 0.3	0.08 ± 0.04	2.5 ± 0.2	0.8 ± 0.2
	ZnS NDS	5.3 ± 1.3	46 ± 3.2	-	3.5 ± 1.2	-	1.8 ± 0.8	-	2.5 ± 1	1 ± 0.6
CIGSSe	ZnS NDS	28.7 ± 0.04	4.2 ± 0.02	-	20.6 ± 0.03	0.03 ± 0.002	46.4 ± 0.06	0.003 ± 0.0006	0.06 ± 0.03	-
	CIGSSe	28.2 ± 0.5	4.2 ± 0.02	-	20.6 ± 0.03	0.03 ± 0.002	46.4 ± 0.06	0.003 ± 0.0006	0.06 ± 0.03	-

These data were calculated separately for each region of interest.

since the Cu overestimation is much higher in In_2S_3 than in CIGSSe because of the higher content of S_2 in In_2S_3 than in CIGSSe. To determine a more accurate value for the composition of the In_2S_3 layer, its mass spectrum was evaluated separately. Overlapping mass peaks were deconvoluted by taking into account the isotope abundance. The values corrected by this procedure are shown for both In_2S_3 and CIGSSe in Table II. We note here that Table II shows deconvoluted values for CIGSSe for a region ~ 100 nm far away from the interface and hence these values cannot be compared with the values shown in Figure 5(a). The aim of this procedure is to show that the composition of CIGSSe in the area near the interface (Figure 5(a)) is very different to that inside the CIGSSe bulk (Table II). This is not the case for In_2S_3 , where the deconvoluted values were determined for a region close to the interface, knowing that the composition of In_2S_3 is rather homogenous within the depth.

Furthermore, at the CIGSSe surface, we observe a distinct zone of about 2.5 nm width marked in gray in Figure 5(a). In this region, the Cu concentration decreases (Cu-depleted atoms = $(1 \pm 0.07) \times 10^{21} \text{ cm}^{-3}$), and the In concentration slightly increases (In enriched atoms = $(1.4 \pm 0.1) \times 10^{21} \text{ cm}^{-3}$ compared with the CIGSSe bulk), whereas the Se and S concentrations remain constant (S coming from CIGSe surface sulfurization [25]). The average composition of this region is 10.3 ± 0.5 at.% Cu, 34.8 ± 0.7 at.% In, and 54.1 ± 1 at.% Se and S. This observation correlated with HRSTEM studies (Figure 3(a)) suggests that this region corresponds to the CuIn_3Se_5 ODC region, even if the composition obtained by APT is slightly different from the stoichiometric one. Indeed, according to Cu_2Se - In_2S_3 pseudobinary phase diagram [26], the Cu concentration in $\beta\text{-CuIn}_3\text{Se}_5$ phase is between 10 and 15 at.%, which fits well with the APT results.

Regarding the impurities, Cl was detected inside the In_2S_3 layer and at the CIGS surface, but it was not segregated at the In_2S_3 /CIGSSe interface. These Cl atoms stem from the incomplete sulfurization of the Cl containing indium oxide precursor film, knowing that the presence of chlorine is beneficial for this type of solar cells. As shown in Table II and Figure 5(a), the Cl concentration in In_2S_3 is in average 2.2 at.%, and it shows a gradient within the first 5 nm of the buffer layer. The Cl gradient can be explained by the fact that the ILGAR layers deposited in the first process cycles see more H_2S from the following cycles than the later ones. Moreover, Cl diffuses to a small extent into the CIGSSe absorber. Na and O impurities were detected in the In_2S_3 buffer layer (0.3 ± 0.06 and 0.1 ± 0.03 at.%, homogeneously distributed), but none of these impurities is segregated at the In_2S_3 /CIGSSe interface. In the case of $\text{CdS}/\text{Cl}(\text{G})\text{Se}$ (with CdS deposited by CBD), O was found to segregate at the p-n junction (~ 0.8 at.%, see [19–21]). This may be correlated with the presence of In or Ga oxides on the surface of the absorber. In the case of ILGAR deposition, Fu *et al.* [12] had shown that HCl gas formed while the sulfurization step attacks these oxides leaving an oxide-free absorber surface, but also the H_2S itself can sulfurize

the oxides. Both processes may explain why no O was detected at the In_2S_3 /CIGSSe interface.

In Figure 5(b), the interdiffusion between In_2S_3 and CIGSSe is less pronounced and this is mainly due to the presence of the ZnS NDs between these two layers. Comparison of the nano-ZnS/ In_2S_3 sample with pure- In_2S_3 sample (Table II) shows that the Cu concentration is lower in In_2S_3 for the nano-ZnS/ In_2S_3 sample, whereas the Cl concentration is higher (the ZnS NDs area is excluded knowing that the NDs are Cl-free, i.e., the Cl source in this area is smaller). Moreover, Cl diffusion in CIGSSe is less pronounced for nano-ZnS/ In_2S_3 sample than for pure- In_2S_3 sample. This proves that the ZnS NDs act as a barrier for the Cu diffusion into the In_2S_3 buffer and Cl diffusion into the CIGSSe absorber. Analyses of the nano-ZnS/ In_2S_3 sample reveal absence of Se in the In_2S_3 buffer layer. This may be explained either by the ZnS NDs, which form a full barrier against Se diffusion in In_2S_3 at 225°C or by the Zn diffusion in the first CIGSSe monolayers. In the latter case, Zn keeps Se or/and S anions to preserve the charge neutrality (the Heat of formation values for ZnS and ZnSe are -45.85 ± 0.2 and -38 ± 2 kcal/mol [27]).

Furthermore, the CIGSSe absorber composition of the nano-ZnS/ In_2S_3 sample shown in Table II is slightly different to that of the pure- In_2S_3 sample. This is not surprising since it is very common that the CIGSSe composition varies from one grain to another even in the same sample as shown in our previous study [28]. Moreover, the APT shows a very local composition (i.e., on a specific grain) and not an overall composition of the absorber.

Figure 6 clearly reveals the 3D distribution of the ZnS NDs between the buffer and the absorber layers. As it is shown in top view map inserted as an inset in Figure 6, these NDs are very close to each other and have an ellipsoidal shape with the thickness of ~ 4 nm (z axis) and the

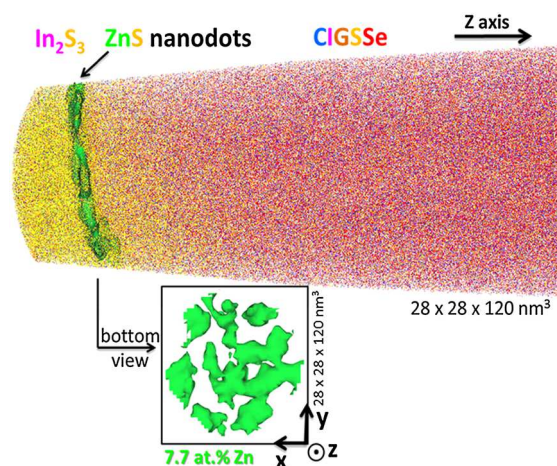


Figure 6. Atom probe tomography 3D map showing the distribution of In (pink), S (yellow), Zn (light green), Cu (blue), Ga (orange), and Se (red). The presence of the ZnS nanodots at the In_2S_3 /Cu(In,Ga)Se₂ interface is clearly shown in the bottom view element envelope map (see inset, 7.7 at.% Zn).

diameter 5–10 nm (x and y axes), information which could not be given by HRSTEM analysis because of the superposition of the NDs within depth of the lamella (2D effect).

The proxigram from Figure 5(b) shows a thin layer (~4 nm in agreement with HR-HAADF from Figure 4) where the Zn concentration is in average 22 at.%. The increase in Zn concentration in this thin layer is in agreement with the EDX measurements (Figure 2(c)). This layer is assigned to the ZnS NDs layer, but also to In_2S_3 found in between the dots. The correct composition of this mixed ZnS- In_2S_3 layer (Table II) is obtained after deconvolution of the overlapping mass peaks, knowing that the mass spectrum of this specific region was evaluated separately. The same procedure was applied to determine the correct averaged composition of the ZnS NDs. In the latter case, due to the small size of the dots, the statistics was poor (low number of atoms per each box, ~1000 ions). This explains the significant standard deviation (2σ with $\sigma = (c_i(1 - c_i)/N)^{1/2}$, where c_i is the calculated atomic fraction of each species i , and N is the total number of the ions) shown in Table II. From the APT data, we clearly observe that these NDs do not consist of pure ZnS, but Cu (3.5 ± 1.2 at.%), In (5.3 ± 1.3 at.%), Se (1.8 ± 0.8 at.%), Cl (1 ± 0.6 at.%), and O (2.5 ± 1 at.%) are present as well. These impurities stem most likely from the In_2S_3 buffer and CIGSSe absorber layers and diffused into the ZnS NDs during the mixed In_2S_3 -ZnS deposition at 225 °C. We note here that ZnS deposition was done using an aqueous solution of Zinc acetylacetonate and not ZnCl_2 , and, therefore, no Cl is expected in the ZnS NDs. This means that the Cl detected in ZnS NDs, which originates from the In_2S_3 deposited in between the dots, is diffusing in the dots during the deposition process at 225 °C. Regarding the Na and O impurities, there is no interfacial segregation at $\text{In}_2\text{S}_3/\text{ZnS}$ or ZnS/CIGSSe interfaces, but these impurities are mostly accumulated inside the In_2S_3 buffer layer, as observed for the previous sample.

Furthermore, at the CIGSSe surface, there is a distinct zone of about 3 nm width marked in gray in Figure 5(b). In this region, the Cu concentration decreases, whereas the In and Zn concentrations both slightly increase. The sum of Se and S concentrations remains constant in the CIGSSe. In this case, the averaged composition of the surface region (12.2 ± 0.5 at.% Cu, 26.25 ± 0.7 at.% In, and 59.4 ± 1 at.% Se and S) does not correspond anymore to CuIn_3Se_5 ODC, as observed for the pure- In_2S_3 reference sample. This may be due either to the ZnS NDs layer, which may act as a barrier against Cu diffusion in In_2S_3 hindering the formation of CuIn_3Se_5 or to the Zn diffusion in the first monolayers of CIGSSe, which may disturb the formation of the ODC (as was observed for the CdS/CI(G)S [19–21]).

Furthermore, the concentration of depleted Cu atoms ($(1.4 \pm 0.1) \times 10^{21} \text{ cm}^{-3}$) is almost equal to the concentration of enriched In and Zn atoms ($(3.1 \pm 0.16) \times 10^{20} \text{ cm}^{-3}$ and $(1.2 \pm 0.09) \times 10^{21} \text{ cm}^{-3}$, respectively). Therefore, we propose that at the CIGSSe surface most of the Cu vacancies are replaced by Zn (Zn_{Cu}^+ donor defects), but also few of them

by In ($\text{In}_{\text{Cu}}^{2+}$ donor defects). The formation of most of these defects is thermodynamically favorable (formation energy of $\text{In}_{\text{Cu}}^{2+}$ and V_{Cu}^- is only 0.22 and 0.75 eV, respectively) as calculated by Guillemoles *et al.* [29]. It is important to mention here that the formation energy for Zn_{Cu}^+ defects in CIGS surface or bulk is unknown in the literature. In the case of CdS/CI(G)S interface, the “missing” Cu ions were nearly identical with the “surplus” Cd ions as shown in our previous studies [19–21]. Indeed, it was proposed that most of the Cu vacancies are occupied by Cd atoms and form Cd_{Cu}^+ donor defects at the CIGS.

To make sure that Zn is present at the surface of the CIGSSe at larger scale, XPS measurements were conducted. In order to make the deeply buried absorber side of the ZnS NDs/CIGSSe heterointerface accessible for characterization, the ZnS NDs were etched off incrementally by dipping the specimen in a diluted HCl solution. The etching time is 1 min, 5 min, 15 min, 1 h and 20 h, respectively. It is important to know that ZnS, when deposited on a Mo substrate, is completely removed already after 15 min etching in a diluted HCl solution [30].

Figure 7 shows how the most prominent Zinc XPS feature, the Zn 2p peak, changes with etching time. The ZnS layer dissolves rapidly in the HCl solution. Even the shortest etching time reduces the ZnS ND layer considerably. However, a small amount of Zn remains on the surface even after etching for an extended time of 20 h. This remaining Zn on CIGSSe cannot be present as a constituent of ZnS. Otherwise, it would be etched away as observed on a Mo substrate. In agreement with APT results, this could be interpreted as a Zn diffusion into the CIGSSe absorber (grains and grain boundaries) where it resists the etching.

Moreover, the Zn XPS peak position of the 20 h-etching sample suggests that the Zn is also bound to S or Se.

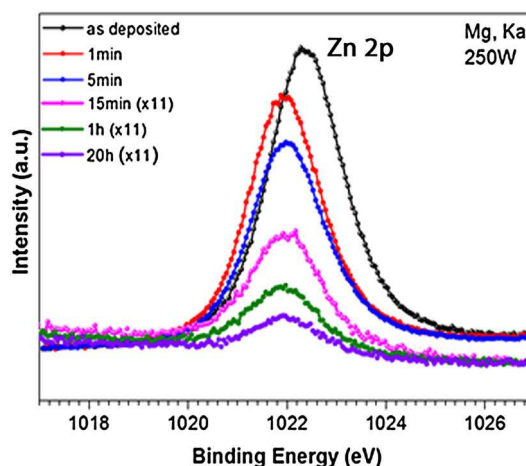


Figure 7. Zn 2p photoemission lines of as-prepared ZnS nanodots on a $\text{Cu}(\text{In,Ga})(\text{Se,S})_2$ (CIGSSe) absorber (black), and the incrementally etched ZnS nanodots on a CIGSSe absorber with aqueous HCl solution. The corresponding etching time is 1 min, 5 min, 15 min, 1 h and 20 h, respectively.

It should be noted that a pronounced shift of the energetic Zn 2*p* position can be observed between as prepared ZnS and all etched samples. In order to check if the shift is due to the change of the chemical environment or not, the modified Auger parameters [31] are computed using the Zn 2*p* core level and the Zn L₃M₄₅M₄₅ Auger signal, $\alpha = E_{\text{kin}}[\text{Zn L}_3\text{M}_{45}\text{M}_{45}(^1\text{G})] + E_{\text{B}}[\text{Zn 2p}]$. The calculated result shows no change in the modified Auger parameters. Therefore, the reason for the shift in the binding energy can be attributed to a band bending or a charging of the sample and can therefore be neglected for our intensity consideration.

4. DISCUSSION

In this work, it had been shown that during In₂S₃ ILGAR deposition at 225 °C, Cu diffusion in In₂S₃ and In diffusion in CIGS_{Se} take place due to the gradient of chemical potential between In₂S₃ and CIGS_{Se}. It is suspected indeed that part of the Cu vacancies, which are present at the CIGS_{Se} surface are replaced by In, whereas Cu may occupy In sites and vacancies in In₂S₃ [32]. Because of the very high mobility of Cu in CIGS and In₂S₃ (higher than In) [32], it is suspected that a Kirkendall effect [33] may take place, which implies the movement of the In₂S₃/CIGS_{Se} interface towards the CIGS_{Se} absorber. On the other hand, in the present work, a Cu-depleted CIGS_{Se} surface was directly put in evidence by APT.

The Cu-depleted region at the surface of polycrystalline chalcopyrite thin films has already been proposed experimentally [34–36] and theoretically [37,38]. There are several models trying to explain the Cu-depleted CIGS surface. First, a so called ODC (or OVC) compound with a concentration ratio of $[\text{Cu}]/([\text{In}] + [\text{Ga}]) = 1/3$ was proposed [37]. First principle calculations confirmed the energetically favorable formation of this compound [37], and its n-type conductivity was explained by Herberholz *et al.* [39] as a consequence of the presence of positive charges that lead to a strong surface band bending. In our correlative HRSTEM-APT studies, we indeed observed the formation of such an ODC compound at the CIGS surface for the pure In₂S₃ reference sample. In the case of nano-ZnS/In₂S₃ sample, the only reason for the absence of the expected ODC may be the presence of ZnS NDs, which may act as a barrier layer for the Cu diffusion from the CIGS_{Se} into In₂S₃, and thus preventing the formation of this compound.

Furthermore, in the work of Mönig *et al.* [35], a novel explanation for the Cu-depleted CIGS surface was presented. On the basis of depth dependent hard XPS results on Cu-depleted Cu(In,Ga)S₂ films, a Cu-depleted (0% [Cu]) surface layer with an extension in depth in the sub-nanometer region was observed. This Cu-depleted surface is the result of a surface reconstruction as predicted by first principle calculations [37,38] and shows a surface band gap measured by scanning tunneling spectroscopy of 1.4 ± 0.2 eV [40], clearly larger than the bulk band gap

of the material investigated. In this work, APT measurements performed on both samples clearly show Cu-depleted CIGS_{Se} surfaces with an extension of 2–4 nm, but no Cu-free layer at the absorber surface as proposed by Mönig *et al.* [40]. It should not be forgotten that the previous discussion involves only as grown chalcopyrite layers. During the In₂S₃ deposition at ~225 °C, Cu diffusion from the absorber into the buffer layer takes place [41–44] for both samples. High-energy photoemission spectroscopy measurements performed on In₂S₃ buffers, PVD-grown on CIGSe absorbers without heating, showed a diffusion of Cu in the buffer layer only after a post annealing at 200 °C for 15–35 min [45]. In fact, this treatment is necessary to achieve high efficiency cells (15.2%, certified by Fraunhofer ISE [46]). The reason for the improvement of the efficiency may be explained as follows: The diffusion of Cu into the buffer layer leaves a Cu-depleted region at the surface promoting the formation of the ODC phase. This compound has a wider band gap than the chalcopyrite phase, which would in turn affect the band line-up positively, increasing the V_{oc} .

For the mixed In₂S₃-ZnS buffer layer, APT and XPS results show a similar behavior: Zn diffuses within the first 2–3 monolayers of the CIGS_{Se} absorber. As for Cd, Zn²⁺ in addition to the In³⁺ may occupy the V_{Cu} sites causing an accumulation of positive charges (Zn_{Cu}^+) that would lead to a downward band bending at the surface. Zn at the CIGS_{Se} surface may act in a similar way as the Cd at the CIGS surface [42], i.e., it pins the Fermi level at the interface close to the conduction band. This configuration is very stable and reduces the recombination rate at the interface, thus improving the overall performance of the device. We note here that neither APT nor HR-HAADF show the formation of $[\text{Cu}_{(1-w)}, \text{Zn}_w]\text{InS}_4$ or $[\text{Zn}_{(1-z)}, \text{Cu}_z]\text{S}$ compounds at the CIGS surface as was suggested by Bär *et al.* [30]. In this work the CIGS_{Se} surface composition detected after peak deconvolution corresponds more to $\text{ZnCu}_3\text{In}_8[\text{Se},\text{S}]_{16}$.

The aim of this work was indeed to understand why the nano-ZnS/In₂S₃ buffered sample shows higher efficiency than the pure In₂S₃ sample. We attribute this effect to the presence of the Zn at the CIGS_{Se} surface which, as observed for the CdS case [19–21], may pin the p–n junction to the conduction band leading to a very stable configuration. The latter one may be indeed more stable than the one characterized by an ODC phase formation at the CIGS surface (observed for pure In₂S₃ sample).

5. SUMMARY AND CONCLUSION

In this work, we investigated the nanostructure and chemistry of the p–n junction region of two solar cell samples with different conversion efficiencies (pure In₂S₃ and the nano-ZnS/In₂S₃). To understand the relationship between the electrical, structural, and chemical properties, correlated TEM, APT, and XPS studies were performed.

For the pure In_2S_3 sample, a CuIn_3Se_5 ordered-defect compound was observed at the CIGSSe surface, whereas for the nano-ZnS/ In_2S_3 sample, no such compound was detected. The absence of an ordered-defect compound in the latter sample was explained either by the presence of the ZnS NDs, which may act as a barrier layer for Cu diffusion in CIGSSe preventing the formation of this compound or by the presence of Zn at the CIGSSe surface, which may disturb the formation of the ODC. For the nano-ZnS/ In_2S_3 specimen, Zn was found in the first monolayers of the absorber layer leading to a downward band bending at the surface. This configuration is very stable (Fermi level pinning at the conduction band) and reduces the recombination rate at the interface, thus improving the overall performance of the device. Na and Cl impurities are preferentially located inside the In_2S_3 buffer layer and not at the interfaces.

The experimental findings of this work demonstrate the capability of correlative TEM-APT-XPS studies in investigating buried interfaces. These studies yield vital information for understanding and designing the p–n junction band structure in CIGS solar cells.

ACKNOWLEDGEMENTS

The authors would like to thank to A. Steigert (HZB) for performing the XPS investigations and to Dr. T. Niesen and Dr. J. Palm (AVANCIS GmbH & Co. KG) for providing the absorber material. This work was funded by Federal Ministry of Education and Research (Contract 03X5522), the German Federal Ministry for the Environment, Nature Conservation and Nuclear safety (Contract 0327657), and Chinese Scholarship Council for the sponsoring of Yanpeng Fu's PhD thesis.

REFERENCES

1. Empa [Internet]. Empa.ch: A new world record for solar cell efficiency, 2013. Available from: <http://www.empa.ch/plugin/template/empa/3/131438/---/l=2> [cited 2013 January 18].
2. Chopra KL, Kainthla RC, Pandya DK, Thakoor AP. Chemical solution deposition of inorganic films. In *Physics of Thin Films*, Hass G, et al. (eds). Academic Press: New York, 1982; 167–235.
3. Ortega-Borges R, Lincot D. Mechanism of chemical bath deposition of cadmium-sulfide thin-films in the ammonia-thiourea system - in-situ kinetic-study and modelization. *Journal of the Electrochemical Society* 1993; **140**: 3464–3473.
4. Naghavi N, Abou-Ras D, Allsop N, Barreau N, Bucheler S, Ennaoui A, Fischer CH, Guillen C, Hariskos D, Herrero J, Klenk R, Kushiya K, Lincot D, Menner R, Nakada T, Platzer-Bjorkman C, Spiering S, Tiwari AN, Torndahl T. Buffer layers and transparent conducting oxides for chalcopyrite $\text{Cu}(\text{In,Ga})(\text{S,Se})_2$ based thin film photovoltaics: present status and current developments. *Progress in Photovoltaics* 2010; **18**: 411–433.
5. Allsop NA, Schonmann A, Belaidi A, Muffler HJ, Mertesacker B, Bohne W, Strub E, Rohrich J, Lux-Steiner MC, Fischer CH. Indium sulfide thin films deposited by the spray ion layer gas reaction technique. *Thin Solid Films* 2006; **513**: 52–56.
6. Fischer CH, Allsop NA, Gledhill SE, Kohler T, Kruger M, Saez-Araoz R, Fu YP, Schwieger R, Richter J, Wohlfart P, Bartsch P, Lichtenberg N, Lux-Steiner MC. The spray-ILGAR (R) (ion layer gas reaction) method for the deposition of thin semiconductor layers: process and applications for thin film solar cells. *Solar Energy Materials & Solar Cells* 2011; **95**: 1518–1526.
7. Fischer CH, Lux-Steiner MC, Möller J, Könenkamp R, Siebentritt S. Verfahren und Anordnung zur Herstellung dünner Metallchalkogenid-Schichten, in German and internat. Pat., Germany, 1998.
8. Gledhill S, Allison R, Allsop N, Fu YP, Kanaki E, Saez-Araoz R, Lux-Steiner MC, Fischer CH. The reaction mechanism of the spray ion layer gas reaction process to deposit In_2S_3 thin films. *Thin Solid Films* 2011; **519**: 6413–6419.
9. Saez-Araoz R, Krammer J, Harndt S, Koehler T, Krueger M, Pistor P, Hergert F, Jasenek A, Lux-Steiner MC, Fischer CH. ILGAR - In_2S_3 buffer layers for Cd-FREE $\text{Cu}(\text{In,Ga})(\text{S,Se})_2$ solar cells with certified efficiencies above 16%. *Progress in Photovoltaics: Research and Applications* 2012; **20**: 855–861.
10. Allsop NA, Camus C, Hansel A, Gledhill SE, Lauer mann I, Lux-Steiner MC, Fischer CH. Indium sulfide buffer/CIGSSe interface engineering: Improved cell performance by the addition of zinc sulfide. *Thin Solid Films* 2007; **515**: 6068–6072.
11. Nakada T, Hongo M, Hayashi E. Band offset of high efficiency CBD-ZnS/CIGS thin film solar cells. *Thin Solid Films* 2003; **431-432**: 242–248.
12. Fu YP, Allsop NA, Gledhill SE, Kohler T, Kruger M, Saez-Araoz R, Block U, Lux-Steiner MC, Fischer CH. ZnS nanodot film as defect passivation layer for $\text{Cu}(\text{In,Ga})(\text{S,Se})_2$ thin-film solar cells deposited by spray-ILGAR (ion-layer gas reaction). *Advanced Energy Materials* 2011; **1**: 561–564.
13. Fu YP, Saez-Araoz R, Kohler T, Kruger M, Steigert A, Lauer mann I, Lux-Steiner MC, Fischer CH. Spray-ILGAR ZnS nanodots/ In_2S_3 as defect passivation/point contact bilayer buffer for $\text{Cu}(\text{In,Ga})(\text{S,Se})_2$ solar cells. *Solar Energy Materials & Solar Cells* 2013; **117**: 293–299.

14. Gault B, Vurpillot F, Vella A, Gilbert M, Menand A, Blavette D, Deconihout B. Design of a femtosecond laser assisted tomographic atom probe. *Review of Scientific Instruments* 2006; **77**: 043705.
15. Allsop NA, Schonmann A, Muffler HJ, Bär M, Lux-Steiner MC, Fischer CH. Spray-ILGAR indium sulfide buffers for Cu(In,Ga)(S,Se)₂ solar cells. *Progress in Photovoltaics* 2005; **13**: 607–616.
16. Brown G, Faifer V, Pudov A, Anikeev A, Bykov E, Contreras M, Wu J. Determination of the minority carrier diffusion length in compositionally graded Cu(In,Ga)Se₂ solar cells using electron beam induced current. *Applied Physics Letters* 2010; **96**: 022104.
17. Thompson K, Lawrence D, Larson DJ, Olson JD, Kelly TF, Gorman B. In situ site-specific specimen preparation for atom probe tomography. *Ultramicroscopy* 2007; **107**: 131–139.
18. Yan YY, Al-Jassim MM. Transmission electron microscopy of chalcogenide thin-film photovoltaic materials. *Current Opinion in Solid State and Materials Science* 2012; **16**: 39–44.
19. Cojocaru-Mirédin O, Choi P, Wuerz R, Raabe D. Atomic-scale characterization of the CdS/CuInSe₂ interface in thin-film solar cells. *Applied Physics Letters* 2011; **98**: 103504.
20. Choi P, Cojocaru-Mirédin O, Wuerz R. Compositional gradients and impurity distributions in CuInSe₂ thin-film solar cells studied by atom probe tomography. *Surface and Interface Analysis* 2012; **44**: 1386–1388.
21. Cojocaru-Mirédin O, Choi P, Wuerz R, Raabe D. Exploring the p-n junction region in Cu(In,Ga)Se₂ thin-film solar cells at the nanometer-scale. *Applied Physics Letters* 2012, **101**: 181603.
22. Hellman OC, Vandenbroucke JA, Rüsing J, Isheim D, Seidman DN. Analysis of three-dimensional atom-probe data by the proximity histogram. *Microscopy and Microanalysis* 2000; **6**: 437.
23. Yoon KE, Noebe RD, Hellman OC, Seidman DN. Dependence of interfacial excess on the threshold value of the isoconcentration surface. *Surface and Interface Analysis* 2004; **36**: 594–597.
24. Vurpillot F, Larson D, Cerezo A. Improvement of multilayer analyses with a three-dimensional atom probe. *Surface and Interface Analysis* 2004; **36**: 552–558.
25. Niesen T, Lerchenberger A, Wendl M, Karg F, Probst V. Flexible Cu (In,Ga)(S,Se)₂ thin film devices on metal foils formed by rapid thermal processing of stacked elemental layers. *Proceedings 19th European Photovoltaic Solar Energy Conference* 2004; 1706–1709.
26. Park JS, Dong Z, Kim S, Perepezko JH. CuInSe₂ phase formation during Cu₂Se/In₂Se₃ interdiffusion reaction. *Journal of Applied Physics* 2000; **87**:3683.
27. Mills, KC. *Thermodynamic data for inorganic sulphides, selenides and teluride*. Publisher Butterworth & Co: England, 1974.
28. Cojocaru-Mirédin O, Choi P, Wuerz R, Raabe D. Atomic-scale distribution of impurities in CuInSe₂-based thin-film solar cells. *Ultramicroscopy* 2011; **111**: 552–556.
29. Guillemoles JF. Stability of Cu(In,Ga)Se₂ solar cells: a thermodynamic approach. *Thin Solid Films* 2000; **361-362**: 338–345.
30. Bär M, Ennaoui A, Klaer J, Kropp T, Saez-Araoz R, Lehmann S, Grimm A, Lauermann I, Loreck C, Sokoll S, Schock HW, Fischer CH, Lux-Steiner MC, Jung C. Intermixing at the heterointerface between ZnS/Zn(S,O) bilayer buffer and CuInS₂ thin film solar cell absorber. *Journal of Applied Physics* 2006; **100**: 064911.
31. Wagner CD. Chemical-shifts of Auger lines and Auger parameter. *Faraday Discussions* 1975; **60**: 291–300.
32. Abou-Ras D. Structural and chemical analyses of buffer layers in Cu(In,Ga)Se₂ thin-film solar cells. *PhD thesis* 2005; 97–98.
33. Tiwari GP, Mehrotra RS. Kirkendall effect and mechanism of self-diffusion in B2 intermetallics compounds. *Metallurgical and Materials Transactions A* 2012. DOI: 10.1007/s11661-012-1199-0
34. Schmid D, Ruckh M, Grunwald F, Schock HW. Chalcopyrite/defect chalcopyrite heterojunctions on the basis of CuInSe₂. *Journal of Applied Physics* 1993; **73**: 2902.
35. Mönig H, Fischer CH, Caballero R, Kaufmann CA, Allsop N, Gorgoi M, Klenk R, Schock HW, Lehmann S, Lux-Steiner MC, Lauermann I. Surface Cu depletion of Cu(In,Ga)Se₂ films: an investigation by hard X-ray photoelectron spectroscopy. *Acta Materialia* 2009; **57**: 3645.
36. Bär M, Repins I, Contreras MA, Weinhardt L, Noufi R. Chemical and electronic surface structure of 20%-efficient Cu(In,Ga)Se₂ thin film solar cell absorbers. *Applied Physics Letters* 2009; **95**: 052106.
37. Zhang SB, Wie SH, Zunger A. Stabilization of ternary compounds via ordered arrays of defect pairs. *Physical Review Letters* 1997; **78**: 4059.
38. Jaffe JE, Zunger A. Defect-induced nonpolar-to-polar transition at the surface of chalcopyrite semiconductors. *Physical Review B* 2001; **64**(26): 241304.
39. Herberholz R, Rau U, Schock HW, Halboom T, Gödecke T, Ernst F. Phase segregation, Cu migration and junction formation in Cu(In,Ga)Se₂. *European Physical Journal Applied Physics* 1999; **6**: 131.
40. Mönig H, Caballero R, Kaufmann CA, Schmidt TL, Lux-Steiner MC, Sadewasser S. Nanoscale investigations of the electronic surface properties of Cu(In,Ga)

- Se₂ thin films by scanning tunneling spectroscopy. *Solar Energy Materials & Solar Cells* 2011; **95**: 1537.
41. Lei C, Duch M, Robertson IM, Rockett A. Effects of solution-grown on Cu(In,Ga)Se₂ grain boundaries. *Journal of Applied Physics* 2010; **108**: 114908.
 42. Liao D, Rockett A. Cd doping at the CuInSe₂/CdS heterojunction. *Journal of Applied Physics* 2003; **93**: 9380.
 43. Nakada T. Nano-structural investigations on Cd-doping into Cu(In,Ga)Se₂ thin films by chemical bath deposition process. *Thin Solid Films* 2000; **361-362**: 346–352.
 44. Ramanathan K, Noufi R, Granata J, Webb J, Keane J. Prospects for in situ junction formation in CuInSe₂ based solar cells. *Solar Energy Materials & Solar Cells* 1998; **55**: 15–22.
 45. Pistor P, Allsop N, Braun W, Caballero R, Camus C, Fischer C, Gorgoi M, Grimm A, Johnson B, Kropp T, Lehmann S, Mönig H, Schorr S, Weber A, Klenk R. Cu in In₂S₃: interdiffusion phenomena analysed by high kinetic energy X-ray photoelectron spectroscopy. *Physica Status Solidi A* 2009; **206**: 1059.
 46. Pistor P, Caballero R, Hariskos D, Izquierdo-Roca V, Wächter R, Klenk R. Quality and stability of compound indium sulphide as source material for buffer layers in Cu(In,Ga)Se₂ solar cells. *Solar Energy Materials and Solar Cells* 2008; **93**: 148.